



Communication

Acquisition of the Wide Swath Significant Wave Height from HY-2C through Deep Learning

Jichao Wang¹ , Ting Yu¹, Fangyu Deng¹ , Zongli Ruan¹ and Yongjun Jia^{2,*}

¹ College of Science, China University of Petroleum, Qingdao 266580, China; wangjc@upc.edu.cn (J.W.); s20090010@s.upc.edu.cn (T.Y.); b21090010@s.upc.edu.cn (F.D.); ruanzl@upc.edu.cn (Z.R.)

² National Satellite Ocean Application Service, Beijing 100081, China

* Correspondence: jiayongjun@mail.nsoas.org.cn

Abstract: Significant wave height (SWH) is of great importance in industries such as ocean engineering, marine resource development, shipping and transportation. Haiyang-2C (HY-2C), the second operational satellite in China's ocean dynamics exploration series, can provide all-weather, all-day, global observations of wave height, wind, and temperature. An altimeter can only measure the nadir wave height and other information, and a scatterometer can obtain the wind field with a wide swath. In this paper, a deep learning approach is applied to produce wide swath SWH data through the wind field using a scatterometer and the nadir wave height taken from an altimeter. Two test sets, 1-month data at 6 min intervals and 1-day data with an interval of 10 s, are fed into the trained model. Experiments indicate that the extending nadir SWH yields using a real-time wide swath grid product along a track, which can support oceanographic study, is superior for taking the swell characteristics of ERA5 into account as the input of the wide swath SWH model. In conclusion, the results demonstrate the effectiveness and feasibility of the wide swath SWH model.



Citation: Wang, J.; Yu, T.; Deng, F.; Ruan, Z.; Jia, Y. Acquisition of the Wide Swath Significant Wave Height from HY-2C through Deep Learning. *Remote Sens.* **2021**, *13*, 4425. <https://doi.org/10.3390/rs13214425>

Academic Editors: Zhenwei Shi, Bin Pan and Shuo Yang

Received: 8 October 2021

Accepted: 1 November 2021

Published: 3 November 2021

Publisher's Note: MDPI stays neutral with regard to jurisdictional claims in published maps and institutional affiliations.



Copyright: © 2021 by the authors. Licensee MDPI, Basel, Switzerland. This article is an open access article distributed under the terms and conditions of the Creative Commons Attribution (CC BY) license (<https://creativecommons.org/licenses/by/4.0/>).

Keywords: HY-2C; deep learning; the wide swath significant wave height

1. Introduction

Significant wave height (SWH) is the most widely utilized wave parameter in climate assessment and various marine industries. Providing in situ observations, wave buoys are traditional measurement tools of SWH that can provide diverse and comprehensive information and are studied extensively in research [1–3]. However, the single-point measurement has sparse, irregular, and limited spatial coverage, thus, wider spatial coverage is of general interest. Satellite altimeters can quickly and accurately measure the global sea surface height, and their measurement accuracy has reached the centimeter level. The acquired SWH from Geosat [4], Jason-1 and Envisat [5], SARAL/AltiKa [6–8], Sentinel 3A and 3B [9,10], Haiyang-2 series [11–14], Chinese–French Oceanography Satellite (CFOSAT) [15,16] altimeter (ALT) are validated by comparisons with data from the National Data Buoy Center buoys. For ALT data, the measurements remain restricted to the nadir tracks, which greatly limits the number of observations.

Haiyang-2C (HY-2C), China's third marine dynamic environment satellite, is a key component of the HY-2 marine remote sensing satellite series. HY-2C carries visible/infrared and microwave sensors, with high-precision orbit measurement, orbit determination capabilities, and all-weather, all-day, and global detection capabilities. Thus, it provides support for marine resource development, marine environmental protection, and national defense construction, etc.

Deep learning is a class of efficient algorithms for learning representative and discriminative input features in a hierarchical manner [17], which has become a hot topic in various fields, particularly in marine remote sensing, such as classifying oceanographic objects from Synthetic Aperture Radar (SAR) data [18], retrieving sea surface wind speed in SAR images [19,20], providing higher accuracy wave parameters [21–23], etc. It is worth noting

that Wang et al. [24] developed a deep learning approach for retrieving the SWH over an extended swath via a CFOSAT with simultaneous wind and wave observations. We attempt to find a more specific deep neural network using fewer input features to retrieve a wider swath of SWH. The gated recurrent unit (GRU) network is designed to solve the gradient disappearance problem that occurs in a standard recurrent neural network, and is a popular and creditable choice because of its simple structure, fast training speed, and superior effect.

In this paper, we adopt a deep learning method to obtain a wide swath SWH from simultaneous observations of radar ALT and microwave scatterometer (SCA) of HY-2C. First, the nadir SWH obtained by ALT is employed to select the wind speed of SCA, where the time difference is less than 5 s, and we spatially choose the closest wind column. Approximately eight months (from 25 September 2020 to 1 June 2021) of the HY-2C and ERA5 collected datasets are considered and matched. In the configuration cases, the matching criteria are set within a 100 km spatial window and a half an hour temporal window. Then, the test set is divided by a length of 300, and the statistical results are analyzed through the leftmost, center and rightmost columns located in the wide swath SWH, in order to illustrate the performance of the wide swath SWH model in each segmented interval. Finally, the results of the 1-day test set at 10 s intervals are discussed, and two small areas are selected and drawn separately to demonstrate the testing effect of the wide swath SWH model at different ranges of numerical variation.

The structure of this paper can be summarized as follows: Section 2 introduces the characteristics of HY-2C and ERA5, as well as the adopted method and datasets; Section 3 compares and analyzes the performance of the model; finally, Section 4 concludes this paper.

2. Data and Method

Haiyang-2C (HY-2C) was successfully launched on 21 September 2020 at the Jiuquan Satellite Launch Center in Inner Mongolia, China. Unlike the HY-2B satellite in a polar orbit, the HY-2C satellite operates in an inclined orbit [25], which travels at an altitude of 1336 km and presents an orbital inclination angle of 66° . Thus, it achieves the purpose of accelerating satellite revisit to the area within 70 degrees north–south from the equator, shortening the observations interval of the region, and improving the observation's efficiency. HY-2C, the first large-scale remote sensing satellite in an inclined orbit, was constructed under the National Civil Space Infrastructure Plan [26]. The satellite adopts an orbit with regression periods of 10 days and 400 days in the early and later stages, respectively.

The main function of the ALT is to measure the global sea surface height, SWH and gravity field parameters, and the ALT has an external calibration working mode that can cover the complete calibration area. It operates in two frequencies, 13.58 GHz and 5.25 GHz, its pulse-limited footprint is more than 2 km, and the range accuracy of the marine nadir point is more than 2 cm. Although the HY-2C ALT provides SWH in Ku- and C-bands, we select only Ku-band measurements for experimental data in this paper due to their higher accuracy, and the fact that the C-band is designed mainly to modify the path delay caused by ionosphere during Ku-band ALT [27].

HY-2C carries a Ku-band rotating pencil-beam SCA in a non-sun-synchronous orbit. As the main payload in a marine dynamic environment, SCA has a coverage rate of not less than 90% in a global sea area for 1 to 2 days. Its main function is to measure the wind vector field (Figure 1), and the accuracy of wind direction and wind speed measurements are more than 15° and 1.5 m/s, respectively. It also has an external calibration working mode with an operating frequency of 13.256 GHz and two beams; horizontal polarization for the internal beam, and vertical polarization for the external beam. Moreover, Wang et al. [28] verified the wind product of the SCA and confirmed its great availability.

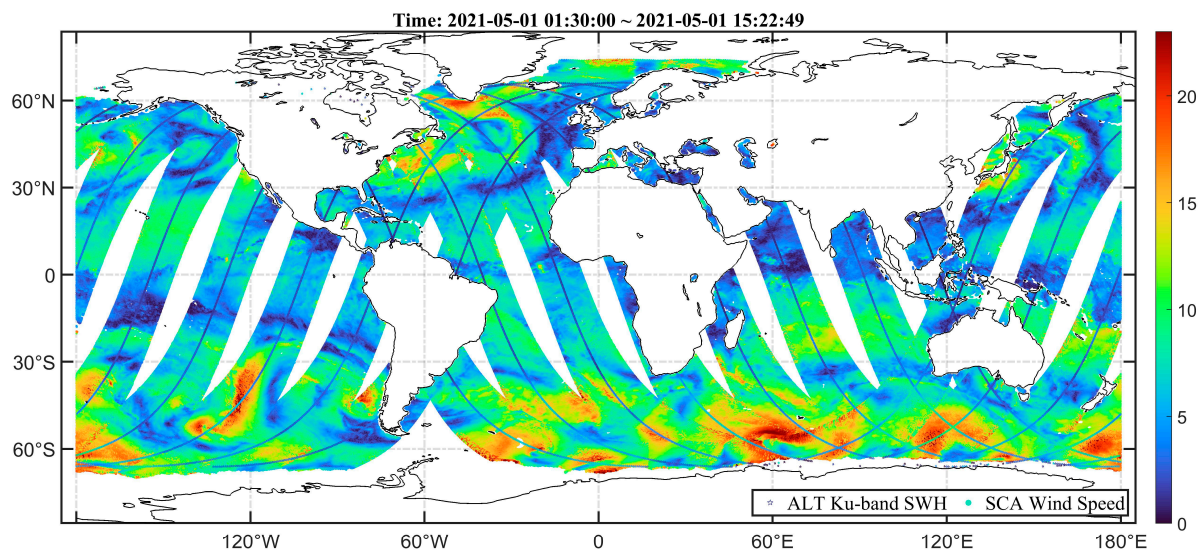


Figure 1. Wind speed information from SCA and the Ku-band SWH from ALT are obtained simultaneously from HY-2C on 1 May 2021.

ERA5 is a global climate reanalysis dataset released by the European Center for Medium-Range Weather Forecasts. It has the advantages of high spatial resolution, hourly atmospheric, terrestrial and ocean climate variables, 3-hourly uncertainty information, more satellite observations, and access to all input observations [29]. The SWH is collected hourly and has a resolution of 0.25° longitude by 0.25° latitude in space.

The wind and wave remote sensing data and the wave analysis datasets have different types of properties, and these are regarded as necessary features and labels for the purpose of verifying the effectiveness of the data. Therefore, the SWH of ERA5 are compared with the observations of HY-2C ALT, and the wind speeds of ERA5 are by compared with SCA L2B products, as shown in Figure 2.

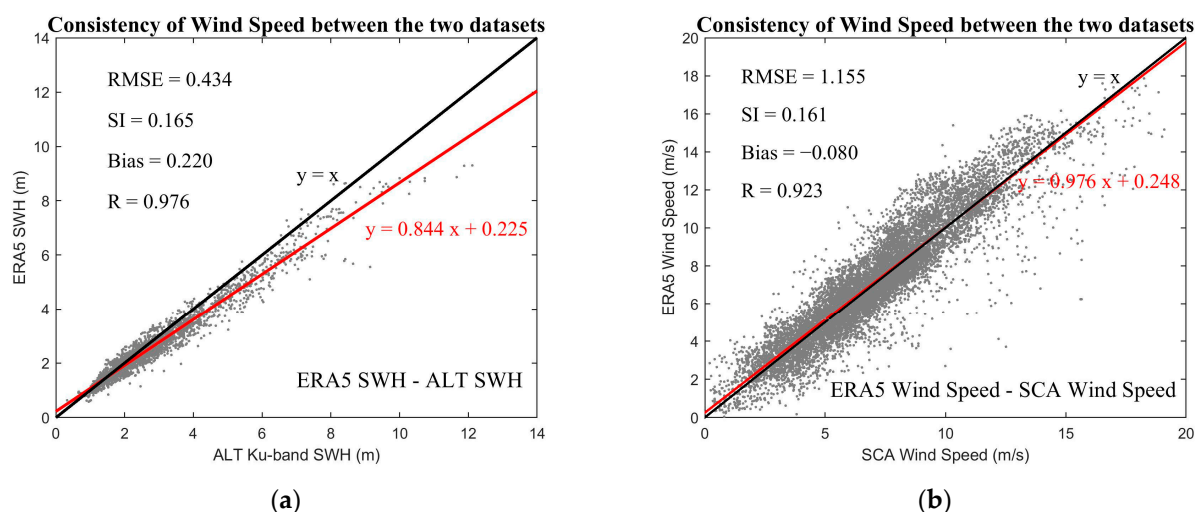


Figure 2. Scatter plots of SWH (a) and wind speed (b) from HY-2C and ERA5 to check the consistency. The red lines indicate the linear fit and the black lines mean the full correlation.

It can be seen that both SWH and wind speed show great consistency, indirectly indicating that it is reasonable to use matched ERA5 SWH as labels at the space and time scales, further proving the feasibility of the model. The statistical metrics, namely, root mean square error (RMSE), scattering index (SI), bias (Bias), and the Pearson correlation

coefficient (R), are applied to measure the effectiveness of the data and model, defined as Equation (1):

$$\begin{aligned} RMSE &= \sqrt{\frac{1}{N} \sum_{t=1}^N (y_o^t - y_v^t)^2} \\ SI &= RMSE / \text{mean}(y_o) \\ Bias &= \sum_{t=1}^N (y_o^t - y_v^t) \\ R &= \frac{\sum_{t=1}^N (y_o^t - \text{mean}(y_o)) (y_v^t - \text{mean}(y_v))}{\sqrt{\sum_{t=1}^N (y_o^t - \text{mean}(y_o))^2} \sqrt{\sum_{t=1}^N (y_v^t - \text{mean}(y_v))^2}} \end{aligned} \quad (1)$$

where y_v^t and y_o^t are tests and observations, respectively.

Deep learning approaches are capable of handling various problems and have been widely applied in various directions. Its attached GRU model possesses two unique gating devices, the reset gate r_t and the update gate z_t , to make a selection between the input x_t and the state of the hidden layer unit at the previous moment h_{t-1} , enabling the model to preserve important features in the long-term sequence (Figure 3a). The reset gate r_t determines the chosen characteristics of combining x_t with h_{t-1} , and its expression is shown in Equation (2).

$$r_t = \sigma(U_r x_t + W_r h_{t-1}) \quad (2)$$

Both x_t and h_{t-1} implement a linear transformation in which they are multiplied by the corresponding weight matrix. They are summed and then activated by a Sigmoid function which compresses the results to between 0 and 1. The candidate state \tilde{h}_t stores the relevant information for selection and its computational expression is shown in Equation (3).

$$\tilde{h}_t = \tanh(U x_t + r_t \odot W h_{t-1}) \quad (3)$$

The Hadamard product of r_t and $W h_{t-1}$ is calculated, that is, the product of their corresponding element. In Equation (1), we know that the value of r_t ranges from 0 to 1. Thus, when the corresponding r_t of an element is 0 and 1, the information in this element will be completely forgotten and retained, respectively. The update gate z_t defines the information saved from the candidate state \tilde{h}_t to the current moment hidden state h_t (Equation (4)).

$$z_t = \sigma(U_z x_t + W_z h_{t-1}) \quad (4)$$

Finally, the two Hadamard products are added to obtain the final h_t , which mainly extracts the important information from h_{t-1} and \tilde{h}_t (Equation (5)). GRU will not remove the previous information over time; it will retain the relevant information and pass it to the next unit to reduce the risk of gradient disappearance.

$$h_t = z_t \odot h_{t-1} + (1 - z_t) \odot \tilde{h}_t \quad (5)$$

The GRU model consists of five layers of neurons. The weights and biases between the neurons are iterated and updated during the training process, using the adaptive moment estimation optimizer and the mean square error loss function as supervision to create a wide swath model. The main parameters of the model are the batch size, the number of hidden layers, the number of hidden units per layer, the learning rate, and the iterations, which take the values of 20, 3, 20, 0.001, and 500, respectively.

To make the width of the nadir SWH close to the dimension of SCA wind speed, different parameters are considered as inputs, including the nadir SWH, latitude, and longitude acquired by ALT, the wind speed collected by SCA L2B product, as well as swell, wind wave, and SWH obtained by ERA5. SWH and wind speed are acquired simultaneously. However, during the operation of the satellite, there are some special cases, such as at a certain time period or moment, when the SWH is not acquired while the wind speed is retrieved. In response to this case, we first extract the nadir SWH and apply their geographical location and corresponding moment for the selection of the derived wind speed. Both SWH and wind speed are along-track data, and their positions vary

with time. Therefore, under the restriction that the time difference does not exceed ± 5 s, information on the wind speed nearest to the time of the nadir SWH can be obtained. It is worth noting that the wind speed information is generated at a time difference of no more than 5 s (Figure 3b).

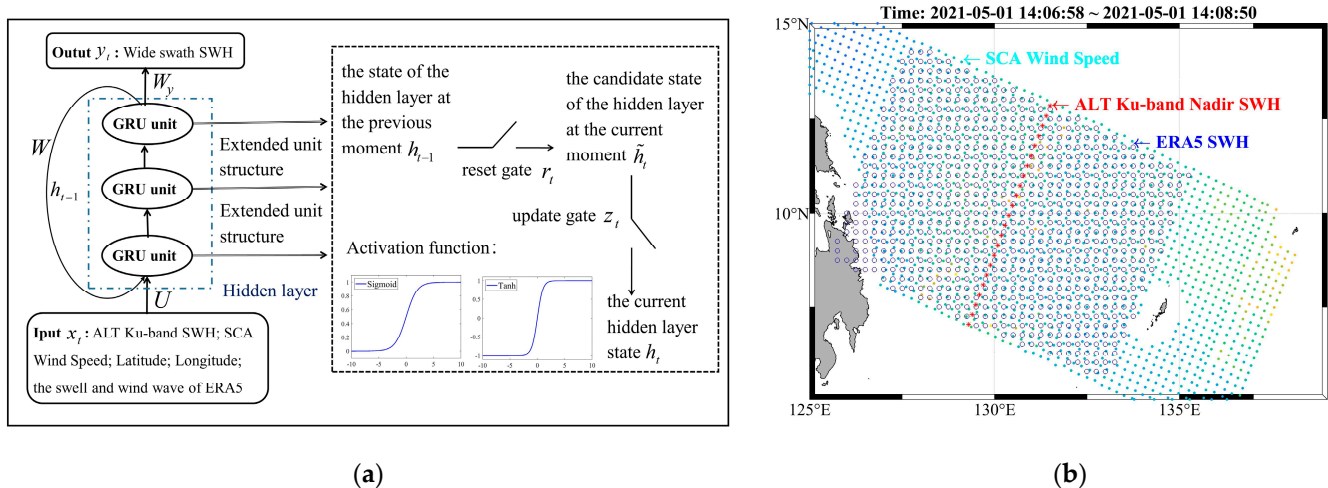


Figure 3. (a) The structure diagram of the GRU network to obtain the wide swath SWH; (b) A schematic diagram of the data parameters and widths acquired by the ALT, SCA, and ERA5. It is worth noting that the widths displayed by ERA5 are selected according to comprehensive consideration of model efficiency and effectiveness.

In addition, the distance between the SCA grid and matched data by ERA5 is limited to less than 100 km and the time window to ± 30 min. Intuitively speaking, the longitude and latitude of the data acquired by HY-2C represent the center of the circle, 100 km denotes the radius, and the longitude and latitude of the ERA5 data within the circle are the candidate points. The distance from the candidate points to the center of the circle is calculated, and the candidate points with the closest distance to the center of the circle are regarded as an approximation of the location of the center of the circle, that is, they are considered as the same point in space. Subsequently, the matching time for this candidate point is selected as the moment closest to the center of circle time within ± 30 min. Similarly, we consider the matched HY-2C and ERA5 data to be identical in time. The width of the matched SWH accounts for half of the wind field in terms of efficiency and benefit.

The latitude range is selected between 60°S and 60°N due to the validity and the large probability distribution of the data. The scope of the training dataset is from 25 September 2020 to 25 April 2021 for seven months of continuous data at 6-min intervals. This paper mainly has two test datasets with similar data volumes. One represents independent 1-month data at 6-min intervals, and the time range is from 1 May 2021 to 1 June 2021, while the other is 1-day data with 10 s intervals, ranging from 1 May to 2 May 2021.

3. Results and Analysis

Wide-dimensional fields have more information and data volume. We utilize the wind speed and SWH simultaneously retrieved by HY-2C as features, and the SWH obtained by ERA5 as labels, so that a wide swath model can be built. It is well known that the ALT data are generated almost per second. Balancing the runtime and the amount of data, we extract the nadir SWH at six-minute intervals and filter the data with a length of 15,360 samples in the training set. Meanwhile, for the test set, we execute the same operation with an integration length of 2500 observations. The swell and wind wave information in ERA5 has a certain effect on the building of wide swath SWH models, for which we gather the relevant data after matching, based on the latitude and longitude of the nadir SWH, and apply them as the input features of Experiments 2 and 3, respectively. The other parameters and settings remain unchanged. The processed datasets are fed into the GRU model; the test set results are shown in Table 1.

Table 1. Numerical results of the test set in the GRU model with different input features.

Input Features of Experiments 1–3	RMSE	SI	Bias	R
Experiment 1: Wind and SWH simultaneously acquired by HY-2C, latitude, and longitude	0.4056	0.1528	0.0154	0.9428
Experiment 2: Wind and SWH simultaneously acquired by HY-2C, latitude; longitude, and swell obtained from ERA5	0.3696	0.1381	−0.0069	0.9530
Experiment 3: Wind and SWH simultaneously acquired by HY-2C, latitude, longitude, and wind wave collected from ERA5	0.4344	0.1629	0.0032	0.9353

Table 1 depicts that the swell presents a positive influence on the establishment of the wide swath SWH model, and conversely, the wind wave has a negative impact on it. For example, compared to the RMSE of Experiment 1, that of Experiment 2 decreases by 0.0360 m, which indicates that model performance has improved, while that of Experiment 3 increases by 0.0288 m, implying a more inefficient model output. The wind-wave mainly exhibits sharp peaks, which are prone to wave breaking when the wind remains strong, while the swell presents smoother peaks, with long and regular wave lines. The wide swath SWH model concentrates on long-term features in the process of learning wind and wave characteristics, while for wind-wave, it behaves as local features. Overall, we mainly focused on the first two experiments in the following analysis.

Three columns of data with a length of 300 on the leftmost, center, and rightmost sides of the wide swath SWH are selected as representatives to further analyze the performance of different stages. In Table 2, the statistics from Experiment 1 show that the center column has better results than the other two columns under arbitrary segmented data. The reason for this phenomenon may be that the larger the distance between either side of the nadir SWH and the center, the less important wind is in the modeling process, and, therefore, there is a worse effect on the nadir SWH.

In the segmented data, the test results of the three columns for Interval 1 are the worst among those for all intervals. For Interval 5, its leftmost and rightmost columns show superior values, its center column is excellent and second only to the center column for Interval 4. We count the total number of points with SWH less than 1 m (troughs) and greater than 7 m (peaks) for each phase. Results indicate that Interval 1 has 332 minimal and maximal points, and these local features gradually disappear during the process of training, resulting in inferior performance. Surprisingly, Interval 5 has only 85 extreme points, thus dominating the results. Based on the above analysis, Interval 5 (in bold), which is located in the middle of the test set and remains superior, is selected to display the range and performance of the three columns of data, as shown in Figure 4.

Comparing Figure 4a–c, it can be found that the center column can accurately estimate the peaks, while SWH on the leftmost and rightmost columns are generally underestimated at the peaks, which indicates that the center column performs better than the other two columns. In addition, the leftmost column, which does not have a SWH greater than 7 m compared to the rightmost and central columns, produces the worst fitting effect and numerical results (Table 2). The reason for this phenomenon may be that the peak information retained in the previous intervals causes an overestimation for some of the current peaks. Although the red line is not as significant as the blue line in Figure 4b for some peaks, it has a better fit between 1 and 5 m. To summarize, the results of the segmented interval in the three columns of data have acceptable performance, given the effectiveness of the model. To distinctly demonstrate the accuracy of the model, the test results for 1 day (from 1 May to 2 May 2021) with 10 s intervals, are plotted in Figure 5.

From Figure 5a, it can be found that the data are distributed with a high probability between 1 and 5 m, and the values are generally larger than 5 m around 60°S. The numerical change in Experiment 1 (Figure 5b) is consistent with the observations in Figure 5a. It is worth noting that the detailed changes in the SWH are not directly visible in the global

area map. This is also the case for Experiment 2 (not shown). Two regions located in the northwest (130–110°W, 10–30°N) and southeast (110–140°E, 60–40°S) are drawn to manifest the detailed value intervals of the wide swath SWH, respectively. Figure 5d,e fluctuate within a small range; the former has a difference of approximately 0.3 m compared to Figure 5c, while the latter demonstrates a high consistency with Figure 5c. Combining with Figure 5f, Figure 5g exhibits better performance than Figure 5h at larger values, which coincides with the phenomena reflected in Figure 4b. Figure 5g declares the expansion of the nadir SWH to generate a real-time grid product with a wide swath along-track, which can be employed as input for wave assimilation, spatial-temporal forecasting, extreme analysis, and so on. Of course, it is undeniable that additionally considering swell in the input characteristics has a promising result when real-time is not strictly required. Furthermore, compared with Figures 1 and 2b, our results extend the width of SWH to half that of the wind field dimension, which demonstrates the effectiveness and feasibility of the model.

Table 2. The numerical results of the segmented data on the leftmost, center, and rightmost columns in Experiment 1. The Interval 5 (in bold) is selected to display the range and performance of the three columns of data.

Segmented Data in the Test Set		RMSE	SI	Bias	R
Interval 1: 1–300	The leftmost column	0.6785	0.2633	0.0210	0.8449
	The center column	0.6023	0.2319	−0.0079	0.8931
	The rightmost column	0.7392	0.2813	−0.0524	0.8280
Interval 2: 301–600	The leftmost column	0.4650	0.1740	−0.0277	0.9280
	The center column	0.2577	0.0966	0.0351	0.9797
	The rightmost column	0.5155	0.1928	−0.0018	0.9041
Interval 3: 601–900	The leftmost column	0.4632	0.1725	−0.0038	0.9335
	The center column	0.2862	0.1064	0.0323	0.9779
	The rightmost column	0.4687	0.1716	−0.0160	0.9333
Interval 4: 901–1200	The leftmost column	0.4623	0.1734	0.0580	0.9293
	The center column	0.2420	0.0891	−0.0137	0.9820
	The rightmost column	0.4484	0.1623	−0.0239	0.9453
Interval 5: 1201–1500	The leftmost column	0.4289	0.1680	0.0244	0.9180
	The center column	0.2554	0.0996	0.0221	0.9731
	The rightmost column	0.4155	0.1591	0.0197	0.9279
Interval 6: 1501–1800	The leftmost column	0.4712	0.1776	0.0426	0.9037
	The center column	0.2844	0.1072	0.0308	0.9688
	The rightmost column	0.4954	0.1843	−0.0100	0.9100
Interval 7: 1800–2100	The leftmost column	0.4438	0.1711	0.0528	0.9128
	The center column	0.2673	0.1034	0.0175	0.9662
	The rightmost column	0.5030	0.1906	−0.0454	0.8819
Interval 8: 2101–2400	The leftmost column	0.5086	0.1875	0.0737	0.9323
	The center column	0.2798	0.1026	0.0610	0.9763
	The rightmost column	0.4834	0.1758	0.0446	0.9268

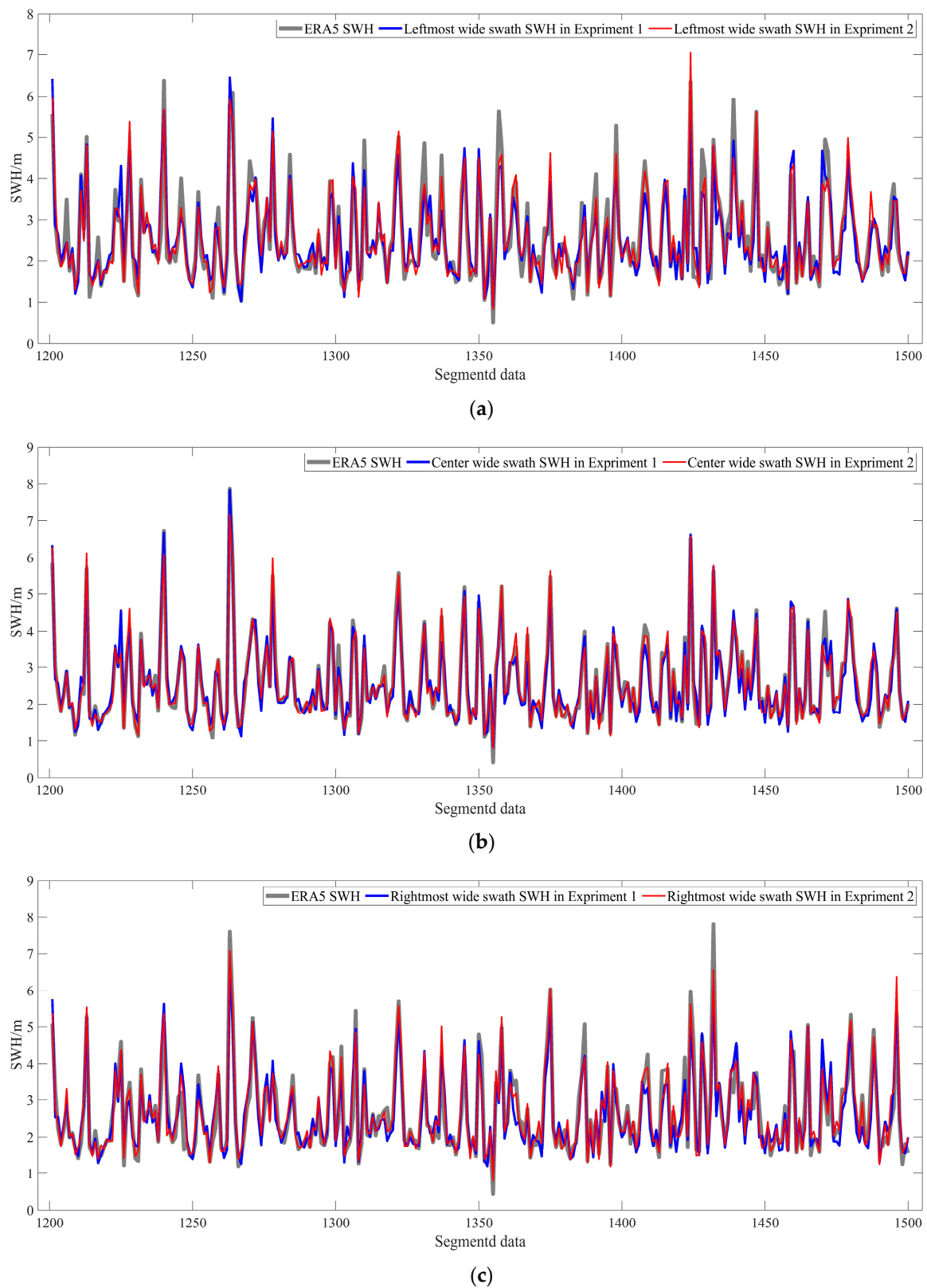


Figure 4. The line graphs for the segmented data. The leftmost, center and rightmost test results of Experiments 1 (blue lines) and 2 (red lines) are denoted in (a–c), respectively.

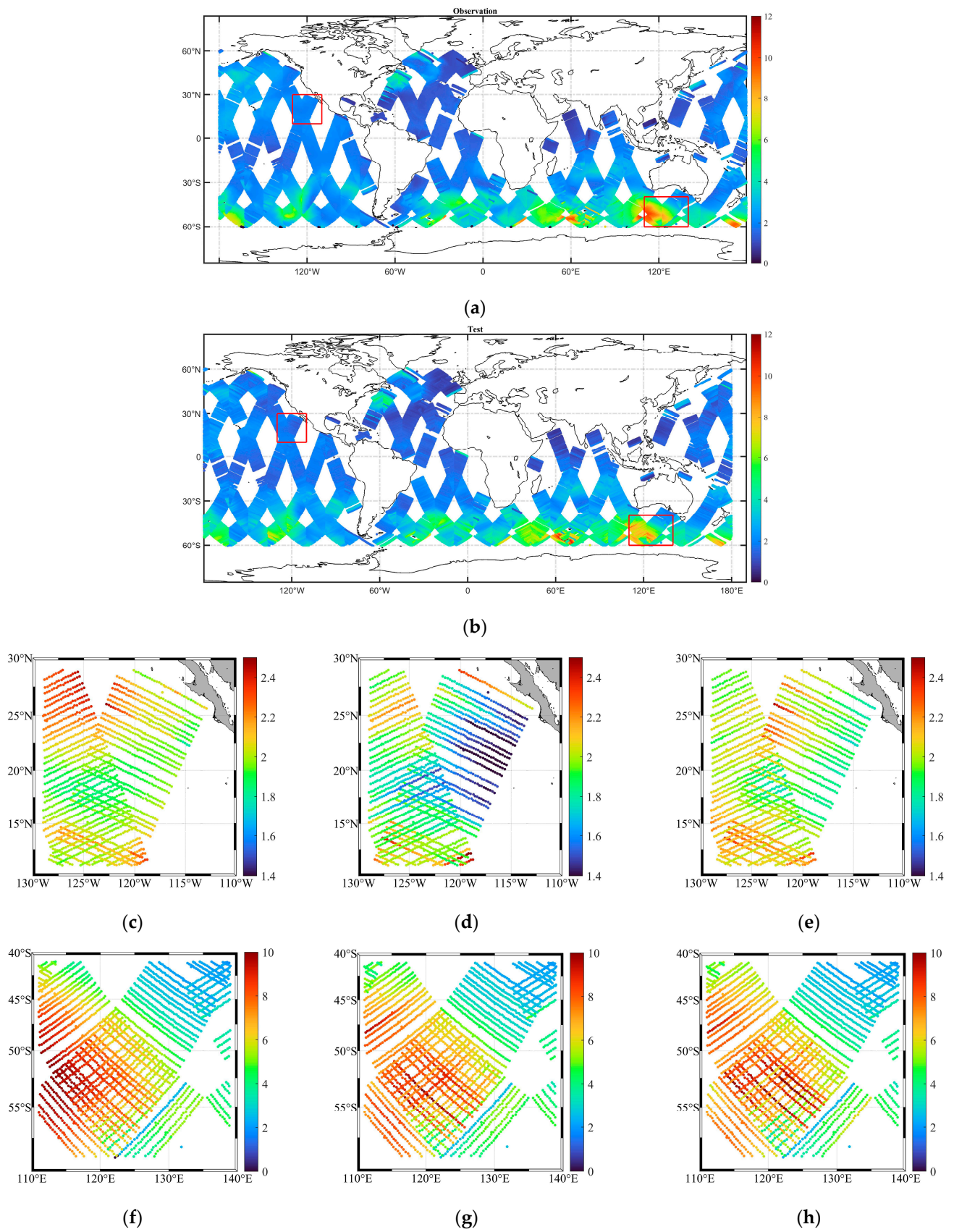


Figure 5. The results of the wide swath SWH. The observation (a) and the test (b) of global-wide swath SWH in Experiment 1, and the observation ((c,f) and the verification ((d,g) in Experiment 1, as well as (e,h) in Experiment 2) of their magnitude plots in the northwestern area and the southeastern area (the red boxes in (a,b)), respectively.

4. Conclusions

This paper employs the use of HY-2C data with simultaneously acquired wind and wave data to build a deep learning model. The gated recurrent unit (GRU) is obtained using a wide swath significant wave height (SWH) field along-track. The Ku-band nadir SWH, as well as its latitude and longitude from the altimeter, are extracted to select the wind columns whose width occupies half of the scatterometer wind field dimension. The SWH of ERA5 is configured based on a temporal window of half an hour and a spatial window within 100 km. The test data are segmented at a length of 300 and the center column outperformed the leftmost and rightmost columns under arbitrary intervals, where the leftmost and rightmost columns are generally underestimated and slightly overestimated at the peaks and the troughs of wide swath SWH, respectively. The test set with a length of 1-day at 10 s intervals is fed into the trained model, and the results show that a better fit appears, considering the swell input in the amplified northwestern area from 1.4 to 2.5 m. Meanwhile, in the southeast, the SWH ranges from 0 to 10 m, and the model performs well without the swell feature for a SWH larger than 7 m. When the data acquired by HY-2C are adopted as features and the data from ERA5 are utilized as the labels, a more time-sensitive grid product along-track is generated. Nevertheless, when the data collected by HY-2C and the swell from ERA5 are applied as features, superior test results are produced. The width of the SWH is extended to half that of the wind field dimension, which could be further expanded or updated by employing deep learning methods according to the demands of the practical situation. The correlative wave parameters may be added appropriately to provide certain relevant information for the training model, so as to generate better grid products.

Author Contributions: Conceptualization, J.W.; methodology, J.W. and T.Y.; software, T.Y.; validation, T.Y.; formal analysis, J.W., Z.R. and Y.J.; investigation, J.W.; resources, Y.J.; data curation, Y.J.; writing—original draft preparation, T.Y.; writing—review and editing, T.Y. and F.D.; visualization, T.Y. and F.D.; supervision, Z.R.; project administration, J.W.; funding acquisition, J.W. All authors have read and agreed to the published version of the manuscript.

Funding: This research was funded by the National Natural Science Foundation of China [grant number 42176011]; the National Key Research and Development Program of China [grant number 2018YFC1406200]; the Shandong Provincial Natural Science Foundation [grant number ZR2020MD060]; the Fundamental Research Funds for the Central Universities [grant number 19CX05003A-5].

Institutional Review Board Statement: Not applicable.

Informed Consent Statement: Not applicable.

Data Availability Statement: Publicly available datasets were analyzed in this study. The altimeter and scatterometer data of HY-2C can be obtained through osdds-ftp.nsoas.org.cn from National Satellite Ocean Application Service. The authors thank the Climate Data Store for providing the abundant high-quality ERA5 data, and these wave measurements can be downloaded from the ERA5 website (cds.climate.copernicus.eu). All accessed data are from 25 September 2020 to 1 June 2021.

Acknowledgments: We thank the National Satellite Ocean Application Service for providing the HY-2C altimeter and scatterometer data (accessible at osdds-ftp.nsoas.org.cn accessed on 7 October 2021). We would also like to thank the Climate Data Store for the data from ERA5 (accessible at cds.climate.copernicus.eu accessed on 7 October 2021).

Conflicts of Interest: The authors declare no conflict of interest.

References

1. Guenaydin, K. The estimation of monthly mean significant wave heights by using artificial neural network and regression methods. *Ocean Eng.* **2008**, *35*, 1406–1415. [[CrossRef](#)]
2. Lin, Y.P.; Huang, C.J.; Chen, S.H. Variations in directional wave parameters obtained from data measured using a GNSS buoy. *Ocean Eng.* **2020**, *209*, 107513. [[CrossRef](#)]
3. Kang, J.; Mao, R.; Chang, Y.; Fu, H. Comparative analysis of significant wave height between a new Southern Ocean buoy and satellite altimeter. *Atmos. Ocean. Sci. Lett.* **2021**, *14*, 100044. [[CrossRef](#)]

4. Dobson, E.; Monaldo, F.; Goldhirsh, J. Validation of Geosat altimeter-derived wind speeds and significant wave heights using buoy data. *J. Geophys. Res. Ocean.* **1987**, *92*, 10719–10731. [[CrossRef](#)]
5. Durrant, T.H.; Greenslade, D.J.M.; Simmonds, I. Validation of Jason-1 and Envisat Remotely Sensed Wave Heights. *J. Atmos. Ocean. Technol.* **2009**, *26*, 123–134. [[CrossRef](#)]
6. Bhowmick, S.A.; Sharma, R.; Babu, K.N.; Shukla, A.K.; Kumar, R.; Venkatesan, R.; Gairola, R.M.; Bonnefond, P.; Picot, N. Validation of SWH and SSHA from SARAL/AltiKa Using Jason-2 and In-Situ Observations. *Mar. Geod.* **2015**, *38*, 193–205. [[CrossRef](#)]
7. Kumar, U.M.; Swain, D.; Sasamal, S.K.; Reddy, N.N.; Ramanjappa, T. Validation of SARAL/AltiKa significant wave height and wind speed observations over the North Indian Ocean. *J. Atmos. Sol.-Terr. Phys.* **2015**, *135*, 174–180. [[CrossRef](#)]
8. Sepulveda, H.H.; Queffeuou, P.; Ardhuin, F. Assessment of SARAL/AltiKa Wave Height Measurements Relative to Buoy, Jason-2, and Cryosat-2 Data. *Mar. Geod.* **2015**, *38*, 449–465. [[CrossRef](#)]
9. Yang, J.; Zhang, J. Validation of Sentinel-3A/3B Satellite Altimetry Wave Heights with Buoy and Jason-3 Data. *Sensors* **2019**, *19*, 2914. [[CrossRef](#)] [[PubMed](#)]
10. Yang, J.; Zhang, J.; Jia, Y.; Fan, C.; Cui, W. Validation of Sentinel-3A/3B and Jason-3 Altimeter Wind Speeds and Significant Wave Heights Using Buoy and ASCAT Data. *Remote Sens.* **2020**, *12*, 2079. [[CrossRef](#)]
11. Chen, C.; Zhu, J.; Lin, M.; Zhao, Y.; Huang, X.; Wang, H.; Zhang, Y.; Peng, H. The validation of the significant wave height product of HY-2 altimeter—primary results. *Acta Oceanol. Sin.* **2013**, *32*, 82–86. [[CrossRef](#)]
12. Wang, J.; Zhang, J.; Yang, J. The validation of HY-2 altimeter measurements of a significant wave height based on buoy data. *Acta Oceanol. Sin.* **2013**, *32*, 87–90. [[CrossRef](#)]
13. Zhang, H.; Qing, W.U.; Chen, G. Validation of HY-2A Remotely Sensed Wave Heights against Buoy Data and Jason-2 Altimeter Measurements. *J. Atmos. Ocean. Technol.* **2015**, *32*, 150402094232008. [[CrossRef](#)]
14. Wang, J.; Aouf, L.; Jia, Y.; Zhang, Y. Validation and Calibration of Significant Wave Height and Wind Speed Retrievals from HY2B Altimeter Based on Deep Learning. *Remote Sens.* **2020**, *12*, 2858. [[CrossRef](#)]
15. Liang, G.; Yang, J.; Wang, J. Accuracy Evaluation of CFOSAT SWIM L2 Products Based on NDBC Buoy and Jason-3 Altimeter Data. *Remote Sens.* **2021**, *13*, 887. [[CrossRef](#)]
16. Li, X.; Xu, Y.; Liu, B.; Lin, W.; He, Y.; Liu, J. Validation and calibration of Nadir SWH Products from CFOSAT and HY-2B with satellites and in situ observations. *J. Geophys. Res. Ocean.* **2021**, *126*, e2020JC016689. [[CrossRef](#)]
17. Zhang, L.; Zhang, L.; Du, B. Deep Learning for Remote Sensing Data: A Technical Tutorial on the State of the Art. *IEEE Geosci. Remote Sens. Mag.* **2016**, *4*, 22–40. [[CrossRef](#)]
18. Bentes, C.; Velotto, D.; Lehner, S. Target classification in oceanographic SAR images with deep neural networks: Architecture and initial results. *IEEE Int. Geosci. Remote Sens. Symp.* **2015**, 3703–3706.
19. Shen, D.; Liu, B.; Li, X. Sea Surface Wind Retrieval from Synthetic Aperture Radar Data by Deep Convolutional Neural Networks. *IEEE Int. Geosci. Remote Sens. Symp.* **2019**, 8035–8038.
20. Qin, T.; Jia, T.; Feng, Q.; Li, X. Sea surface wind speed retrieval from Sentinel-1 HH polarization data using conventional and neural network methods. *Acta Oceanol. Sin.* **2021**, *40*, 13–21. [[CrossRef](#)]
21. Wang, J.K.; Aouf, L.; Dalphin, A.; Li, B.X.; Xu, Y.; Liu, J.Q. Acquisition of the significant wave height from CFOSAT SWIM spectra through a deep neural network and its impact on wave model assimilation. *J. Geophys. Res. Ocean.* **2021**, *126*, e2020JC016885. [[CrossRef](#)]
22. Li, X.; Yang, D.; Yang, J.; Zheng, G.; Han, G.; Nan, Y.; Li, W. Analysis of coastal wind speed retrieval from CYGNSS mission using artificial neural network. *Remote Sens. Environ.* **2021**, *260*, 112454. [[CrossRef](#)]
23. Wang, J.K.; Aouf, L.; Badulin, S. Retrieval of wave period from altimetry: Deep learning accounting for random wave field dynamics. *Remote Sens. Environ.* **2021**, *265*, 112629. [[CrossRef](#)]
24. Wang, J.K.; Aouf, L.; Dalphin, A.; Zhang, Y.G.; Xu, Y.; Hauser, D.; Liu, J.Q. The Wide Swath Significant Wave Height: An Innovative Reconstruction of Significant Wave Heights from CFOSAT’s SWIM and Scatterometer Using Deep Learning. *Geophys. Res. Lett.* **2021**, *48*, e2020GL091276.
25. Pang, D.; Tao, W. HY-2B and HY-2C Operational Satellites under Development. *Aerosp. China* **2016**, *17*, 69.
26. Ren, Y. LM-4B Successfully Launched HY-2C Satellite. *Aerosp. China* **2020**, *21*, 56.
27. Jia, Y.; Lin, M.; Zhang, Y. Evaluations of the Significant Wave Height Products of HY-2B Satellite Radar Altimeters. *Mar. Geod.* **2020**, *43*, 396–413. [[CrossRef](#)]
28. Wang, Z.; Zou, J.; Stoffelen, A.; Lin, W.; Verhoef, A.; Li, X.; He, Y.; Zhang, Y.; Lin, M. Scatterometer Sea Surface Wind Product Validation for HY-2C. *IEEE J. Sel. Top. Appl. Earth Obs. Remote Sens.* **2021**, *14*, 6156–6164. [[CrossRef](#)]
29. Hersbach, H.; Bell, B.; Berrisford, P.; Hirahara, S.; Horányi, A.; Muñoz-Sabater, J.; Nicolas, J.; Peubey, C.; Radu, R.; Schepers, D.; et al. The ERA5 global reanalysis. *Q. J. R. Meteorol. Soc.* **2020**, *146*, 1999–2049. [[CrossRef](#)]